Lattice reconfiguration and phononic band-gap adaptation via origami folding

M. Thota,[1,*] S. Li,[2] and K. W. Wang[1]
[1]*Department of Mechanical Engineering, University of Michigan, Ann Arbor, Michigan 48109, USA*
[2]*Department of Mechanical Engineering, Clemson University, Clemson, South Carolina 29634, USA*

(Received 16 July 2016; revised manuscript received 25 October 2016; published 17 February 2017)

We introduce a framework of utilizing origami folding to redistribute the inclusions of a phononic structure to achieve significant phononic band-gap adaptation. Cylindrical inclusions are attached to the vertices of a Miura-Ori sheet, whose 1 degree-of-freedom rigid folding can enable fundamental reconfigurations in the underlying periodic architecture via switching between different Bravais lattice types. Such a reconfiguration can drastically change the wave propagation behavior in terms of band gap and provide a scalable and practical means for broadband wave tailoring.

DOI: 10.1103/PhysRevB.95.064307

I. INTRODUCTION

By exploiting the fundamental wave phenomena such as reflection and interference in artificially created phononic structures (a host media with periodically distributed inclusions), band gaps could be generated—which are discontinuous spectral regions in the band structure where wave propagation is blocked. Band gaps generated in solid (inclusion)–fluid (host) composite structures are called phononic band gaps (PBGs) and are strongly dependent on the geometry and material properties of the phononic structures [1,2]. The most important geometric property that affects the PBG spectral range and location is the lattice topology (where topology refers to the spatial distribution/configuration of inclusions in this paper). Five distinct two-dimensional (2D) Bravais lattice-types/topologies (oblique, rectangle, center-rectangle, hexagon, and square; see Appendix A) are classified depending on their point-group symmetries, each with fundamentally distinct band structures [3–11]. The dispersion characteristics of these lattice types typically exhibit symmetry-induced band degeneracies which restrict the spectral range of PBGs. As a result, many attempts were made to exploit the correlation between lattice geometry and wave propagation to tailor the PBG via reducing/changing lattice symmetry, either by inserting additional inclusions or via rearranging and reorienting existing inclusions [5,12–23]. However, such efforts were not effective in achieving substantial wave control because the PBG adaptation is only incremental in terms of both spectral range and location, and the mechanisms to realize programmable and controllable topology transformation, especially between different lattice types, are nonexistent. In other words, while it is clear that control over PBG is important and useful in expanding the horizons of various wave control mechanisms with wave energy guiding and trapping across different frequency spectra and enhancing interaction between waves across different physical domains [24–29], the existing state of the art cannot provide versatile and effective wave adaptation.

Towards the goal of bringing on-demand wave tailoring to a new level, here in this research, we develop a paradigm for broadband control of acoustic wave motion by exploring innovations in phononic structures with (a) significant symmetry reduction and versatile topology transformations capable of shifting between different Bravais lattice types and (b) simple/efficient topology reconfiguration mechanisms that are practical to implement. We synthesize a class of reconfigurable phononic structures viz. origami structures that can achieve phenomenal PBG adaption via topology reconfiguration. Our idea here is to exploit origami folding to reconfigure the inclusions of phononic structure between fundamentally different Bravais lattice types. Since the PBG properties are strongly dependent upon the underlying lattice topology, the wave characteristics of these phononic structures can be drastically altered via origami folding and could enable broadband adaptive dispersion characteristics.

II. DESIGN OF ORIGAMI STRUCTURES

The basic ingredient of the proposed origami structure (OS) is an origami sheet that can be folded into exceptionally rich shapes by carefully designing its crease pattern [30–36] and is composed of inclusions attached either on the facets or vertices of the sheet (Fig. 1).

A. Miura-Ori kinematics

The origami sheet is a periodic tessellation of identical degree-4 vertices, which consists of four crease lines that meets at one point. Among the vast many possible origami tessellations—attributed to seven geometric design parameters viz. four crease lengths and three independent angles between them—here in this research we pick a classic design called Miura-Ori that consists of only three independent parameters to construct the OS. Being periodic in nature, the overall kinematics of folding a Miura-Ori sheet can be derived from a vertex unit shown in Fig. 1(d), and the three associated design parameters are the length of the two crease lines (a,b) and the sector angle between these two creases (γ). A dihedral folding angle (θ) is defined between the facet and xy reference plane to characterize the folding configuration, which ranges from being flat ($\theta = 0^\circ$) to fully folded ($\theta = 90^\circ$). Therefore, the outer geometry of the Miura-Ori vertex unit is related to the folding angle as well as the vertex design parameters so that the position of the vertices can be uniquely determined based on Eq. (1). Since the OS design considered in this article has cylindrical inclusions connecting the vertices of two Miura-Ori sheet with air as the host medium [Figs. 1(a)–1(c)], their

---

[*] Author to whom the correspondence should be addressed: mthota@umich.edu

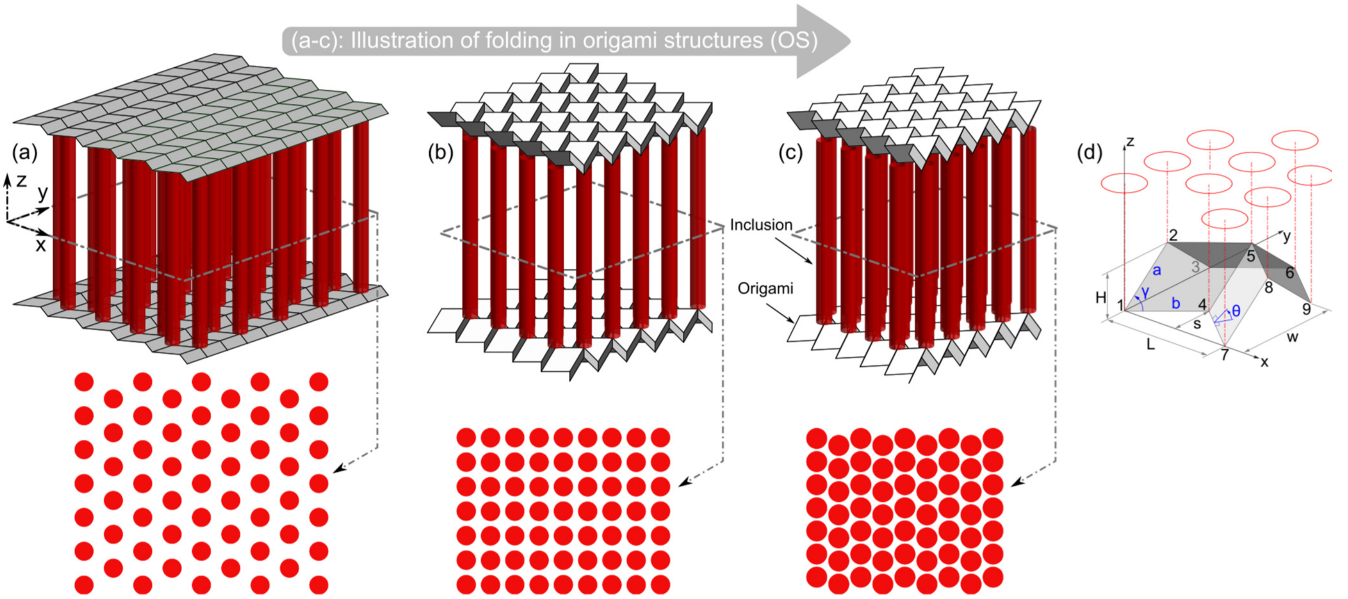

FIG. 1. (a–c) Illustration of folding-induced topology transformation in origami structures (OS). Circular cross-section solid cylindrical inclusions are attached, connecting the vertices of rigid-foldable Miura-Origami sheets with air as the host media; cross-sectional plots in bottom row clearly illustrate topology transformation during folding operation. (d) Miura-Ori unit-vertex parameters.

topology distribution is directly related to the vertices positions projected onto the xy reference plane [red ellipses in Fig. 1(d)]:

$$\begin{aligned} H &= a\sin\theta\sin\gamma, \\ L &= \frac{2b\cos\theta\sin\gamma}{\sqrt{1-\sin^2\theta\sin^2\gamma}}, \\ W &= 2a\sqrt{1-\sin^2\theta\sin^2\gamma}, \\ s &= \frac{b\cos\gamma}{\sqrt{1-\sin^2\theta\sin^2\gamma}}. \end{aligned} \tag{1}$$

B. Parametric analysis

A comprehensive parametric analysis is conducted to survey the achievable lattice topology transformations via Miura-Ori folding. We found that it is possible to redistribute the inclusions between four of the five Bravais lattice types. The only exception is the oblique lattice type that requires a more generic, single collinear degree-4 vertices design, which would not be discussed here:

$$\begin{aligned} A &= \frac{S}{L/2} = \frac{1}{\tan\gamma\cos\theta}, \\ B &= \frac{W/2}{L/2} = \frac{a(1-\sin^2\theta\sin^2\gamma)}{b\cos\theta\sin\gamma} = \frac{a}{b}\cos\gamma\left(A+\frac{1}{A}\right). \end{aligned} \tag{2}$$

For the purpose of parametric study, two dimensionless parameters (denoted as A and B) are defined that correlate the lattice topology to the folding kinematics of Miura-Ori [Eq. (2)]. Assume n is any positive integer, then the hexagonal lattice type requires $A = (2n-1)/\sqrt{3}, B = 2/\sqrt{3}$ (see Appendix B for examples with $n = 1$ and 2), the square requires $A = n, B = 1$, the center-rectangle requires $A/B = n - 1/2$, and the rectangular lattice type requires $A/B = n$. Note that the hexagonal lattice type is a special case of center-rectangular lattice type, and the square is a special case of rectangular lattice type. Based on the formulations above, we find a large range of combinations of sector angle (γ) and crease length ratio a/b, where Miura-Ori folding can enable switching between rectangular and center-rectangular lattice types multiple times [shaded region in the parametric plot of Figs. 2(a) and 2(b)]. When γ and a/b reach specific combinations, one of the center-rectangular (CR) or rectangular (R) configurations becomes a hexagonal (H) or square (S), respectively [dashed curves in Figs. 2(a) and 2(b)]. There exists a subset of γ and a/b combinations (dash-dotted curve) where it's possible to switch between hexagonal (H) and square (S) lattice types. It is not possible to switch between two different square lattice types; however, it is possible to switch between two hexagonal lattice types with different lattice constants [thickened dashed-dotted curve in Fig. 2(a)].

C. Example Miura-Ori design: Lattice topology transformation between hexagon and square

Here we provide a demonstration of an example Miura-Ori design, marked by a triangular crease design in Figs. 2(a) and 2(b), to illustrate the topology transformation between different lattice types during folding. For this particular design the crease lengths $a(= b)$ are assigned to be 0.15 (m) and the sector angle (γ) is 60°. The circular cylindrical inclusions attached to the vertices are made of steel with a radius of 0.041 (m) and the OS is suspended in air (as given in Fig. 1). The longitudinal velocity of sound (c_l) and density (ρ) of cylindrical inclusions (air host) are assumed to be 7850(1.3) (kg/m^3) and 6086(340) (m/s), respectively. Based on the geometric parameters, a maximum folding angle of 71° is possible before the closed packing condition of inclusions is reached. Now, to illustrate the effect of folding operation on the topology of cylindrical inclusions, we plot the 2D cross-section plane of OS transverse to the insertion rod axis

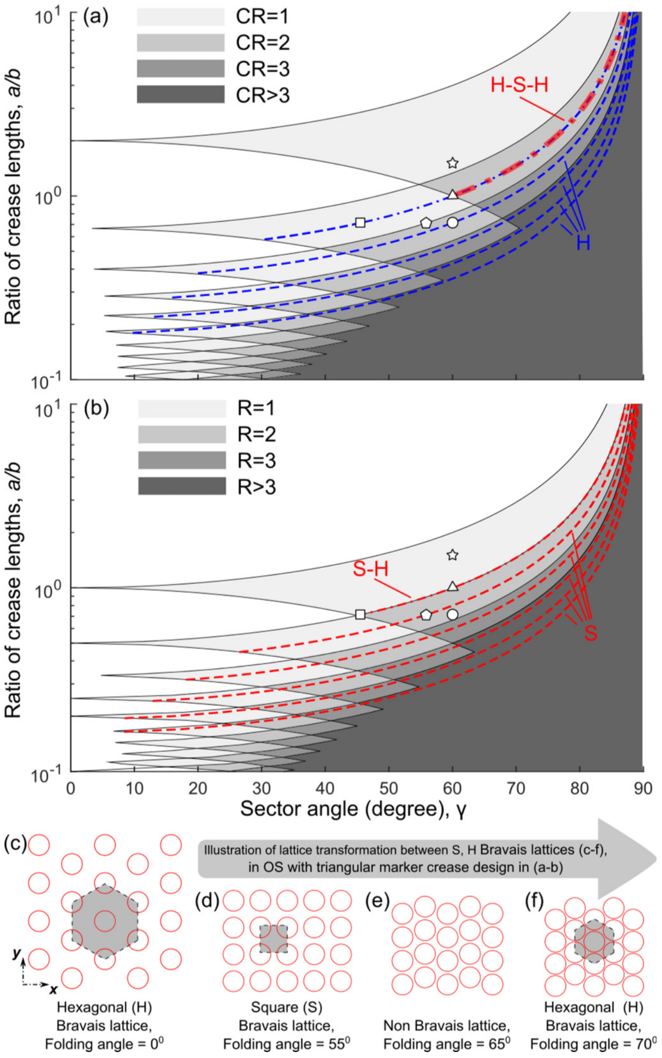

FIG. 2. Achievable Bravais lattice types via Miura-Ori rigid folding based on different crease designs. (a) Combinations of γ and a/b that can achieve center-rectangular (CR) lattice type. White regions correspond to Miura-Ori designs that cannot achieve CR, and the shaded regions correspond to crease designs that can achieve CR multiple times as the Miura folds from $\theta = 0^\circ$ to 90°. For visual clarity, demarcation between Miura-Ori designs that can achieve CR more than 3 times during folding are not plotted separately. Dashed curves in this plot correspond to the subsets of γ and a/b combinations where one of the achievable CR lattice types is actually hexagonal (H). Again for clarity, only the curves based on $n = 1-6$ are plotted. (b) Similar plot as (a), but for rectangular (R) and square (S) lattice types. When considering the topology transformation of a specific Miura-Ori design, both of the two plots need to be considered. In (c–f), we show how folding shifts the lattice configuration between square (S) and Hexagon (H) in OS with a triangular crease design (marked by triangular marker in a and b). Effect of folding on topology transformations corresponding to star, circle, polygon, and square crease designs are provided in Appendix C.

as shown in Figs. 2(c)–2(f). For the considered OS design, the lattice topology of inclusions changes from a hexagon [at 0°, Fig. 2(c)] to square [at 55°, Fig. 2(d)], and finally to hexagon [at 70°, Fig. 2(f)] while transforming into a reduced-symmetry non-Bravais lattice at intermediate angles [e.g., at 65°, Fig. 2(e)] during folding (animation provided in Supplemental Material [37], movie S1). Since the initial configuration is a hexagon, we refer to this particular design as hexagonal-OS.

To realize the folding-induced topology transformation, we have built a unit cell of hexagonal-OS [as shown in Figs. 3(c)–3(e)], composed of a 3D printed Miura-Ori sheet with PVC tubes as inclusions. To build the origami sheet, a *print-stack-assemble* concept is used wherein the individual pieces of the assembly (viz., male facet, female facet, stripe A, and stripe B), shown in Fig. 3(a), are printed separately and assembled to form the origami sheet [Fig. 3(b)]. Custom designed snap-fit hinges on these facets can enable quick assembly and precise folding according to Eq. (1) [Fig. 3(b)]. Moreover, a stripe design is implemented to hold the PVC pipes upright and move them as per the trajectory of origami vertices during the folding process [Fig. 3(b)].

III. WAVE PROPAGTION ANALYSIS

To study the effect of topology transformation on wave transmission through OS, we develop a numerical tool that combines wave propagation theory with origami folding kinematics. The acoustic wave propagation behavior through the 2D plane, transverse to inclusion axis, is evaluated by solving the governing pressure wave equation Eq. (3) with the assumption that the material properties of OS are invariant along the z direction. We represent the periodical repetition of material properties in propagation plane by a primitive unit cell, represented by a dashed rectangle, with lattice vectors $(\vec{a_1}, \vec{a_2})$ and two basis inclusions $(\mathrm{C}_1, \mathrm{C}_2)$ in xy plane, as shown in inset of Fig. 4(a). Furthermore, unit-cell parameters are related to origami unit vertices position via Eq. (4):

$$\left(\frac{1}{\rho {c_l}^2}\right)\frac{\partial^2 p}{\partial t^2} = \nabla \cdot \left(\frac{1}{\rho}\nabla p\right), \tag{3}$$

$$\begin{aligned} \vec{a_1} &= L\hat{x}, \\ \vec{a_2} &= \frac{W}{2}\hat{y}, \\ \vec{C_1} &= \frac{|\vec{a_1}|}{2}\hat{a}_1 + \frac{|\vec{a_2}|}{2}\hat{a}_2, \\ \vec{C_2} &= \left(s - \frac{3|\vec{a_2}|}{2}\right)\hat{a}_2. \end{aligned} \tag{4}$$

A. Plane-wave expansion method

For a given folding angle, the versatile plane-wave expansion (PWE) method [2,3], which can accommodate for spatially varying material properties, is used to evaluate the wave propagation characteristics. Note that because of the large impedance mismatch between the steel inclusion and air host, only longitudinal wave propagation is considered while solving Eq. (3). The fundamental idea behind the PWE method is to expand the periodically varying material properties $\rho_{\mathrm{inv}} = \frac{1}{\rho}$ and $K_{\mathrm{inv}} = \frac{1}{\rho {c_l}^2}$ in Eq. (3) as Fourier series in terms of unit-cell parameters and with plane waves being used as basis functions, as given in Eq. (5), where τ is the place holder for K_{inv} and ρ_{inv}, τ_G being their Fourier coefficient. The wave numbers of the plane waves in the expansion are given

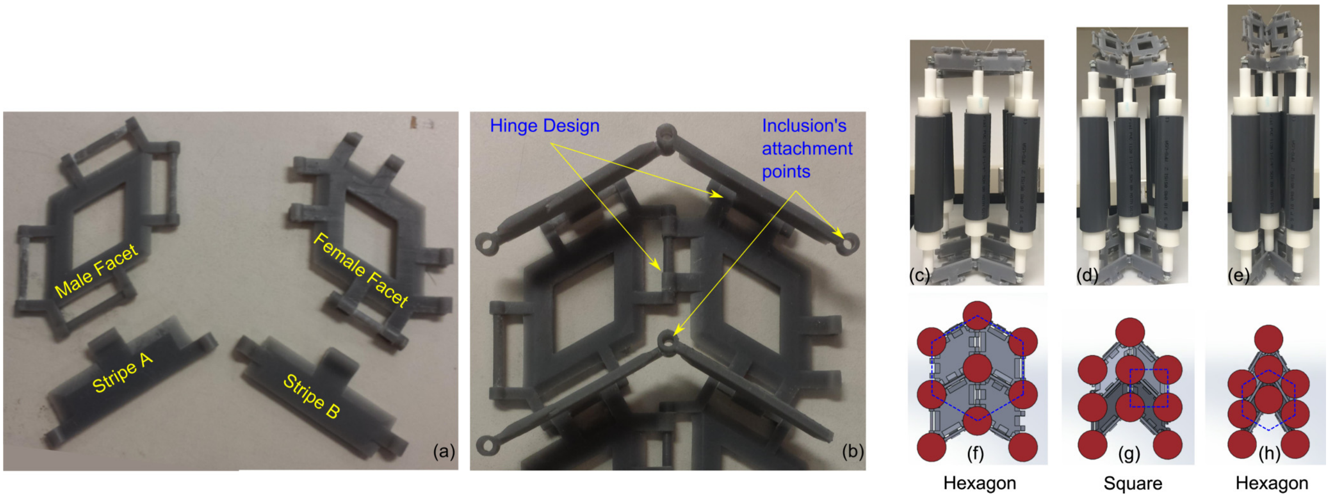

FIG. 3. 3D printed origami sheet. Top view of (a) individual parts and (b) assembled origami sheet. (c–e) Instances of assembled unit cell of hexagonal-OS, illustrating transformation between different lattice types/topologies. (c) Hexagon lattice at 0°. (d) Square lattice at 55°. (e) Hexagon lattice at 70°. (f–h) Reflect the instances of Supplemental Movie [37] S1 at different folding angles corresponding to (c–e).

by reciprocal lattice vectors $\overrightarrow{b_1}$ and $\overrightarrow{b_2}$, with (m, n) being integers, spanning from $-p$ to p:

$$\begin{aligned} \tau(\vec{x}) &= \sum_G \tau_G e^{i\vec{G}.\vec{x}}, \\ \tau_G &= \frac{1}{A_{\text{cell}}} \iint_{A_{\text{cell}}} \tau(\vec{x}) e^{-i\vec{G}.\vec{x}} dA, \\ \vec{G} &= m\overrightarrow{b_1} + n\overrightarrow{b_2}, \\ \overrightarrow{b_1} &= \frac{2\pi}{|\overrightarrow{a_1}|}\hat{x} \quad \& \quad \overrightarrow{b_2} = \frac{2\pi}{|\overrightarrow{a_2}|}\hat{y}. \end{aligned} \tag{5}$$

Now the pressure field in Eq. (3) can also be expanded using the Floquet-Bloch theorem, which states that the wave field in a periodic structure is entirely periodic except for the phase shift across the unit cell, as $p(\vec{x}) = \sum_G p_G e^{i\vec{G}.\vec{x}} e^{i\vec{k}.\vec{x}}$, where $\vec{k}$ is the wave vector. The wave vector is typically swept along the edges of the irreducible first Brillouin zone to evaluate the band-gap structure; for the unit cell considered, the high-symmetry wave vector directions are represented by sides of the rectangle, ΓXMNΓ, with $\Gamma = (0\,0)$, $X = (\frac{\pi}{|\overrightarrow{a_1}|}\,0)$, $M = (\frac{\pi}{|\overrightarrow{a_1}|}\,\frac{\pi}{|\overrightarrow{a_2}|})$, $N = (0\,\frac{\pi}{|\overrightarrow{a_2}|})$, as shown in inset of Fig. 4(a). Further, the Fourier coefficient τ_G in Eq. (5), for circular inclusion, can be simplified as given in Appendix D.

Upon substitution of material properties and pressure field expansions into Eq. (3), Eq. (3) is discretized into the eigenvalue problem (EVP) $[P^{-1}Q - \omega^2 I]p_G = 0$, with P, Q representing $(2p+1)^2$ square matrices, $P_{ij} = K_{\text{inv}_{\vec{G}_i - \vec{G}_j}}$; $Q_{ij} = (\vec{k} + \vec{G}_j)\cdot(\vec{k} + \vec{G}_i)\rho_{\text{inv}_{\vec{G}_i - \vec{G}_j}}$. For the kind of periodic distribution of circular inclusions given in inset of Fig. 4(a),

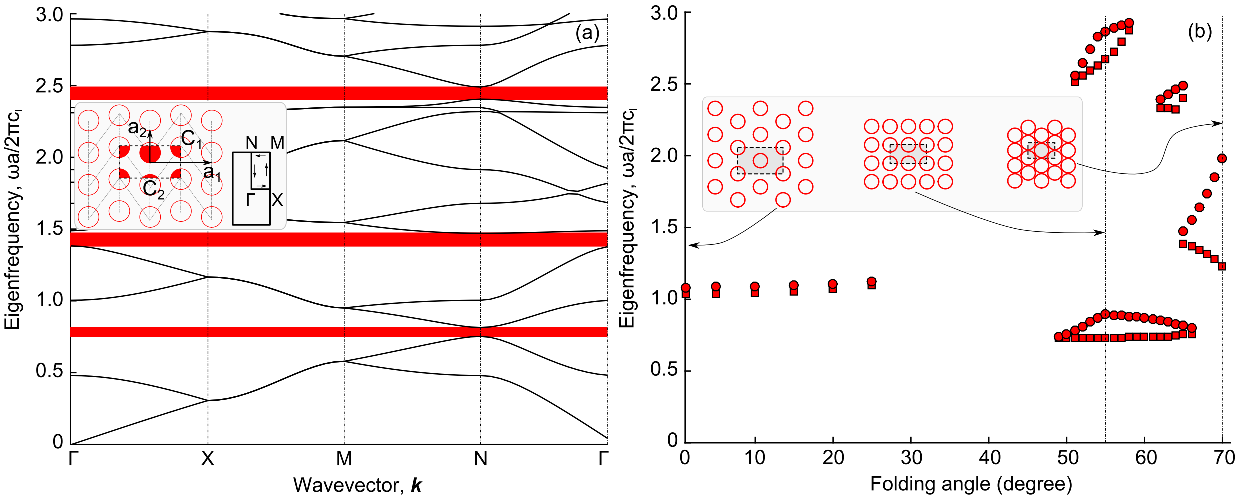

FIG. 4. (a) Band structure of acoustic wave propagation in hexagonal-OS at 65° folding angle with three complete PBGs (horizontal shaded regions). 2D cross section along transverse plane with representative unit cell and first Brillouin zone are given in the inset. (b) Effect of folding on PBGs of hexagonal-OS. Square (circle) markers represent the lower (upper) edge frequencies of PBG. Lattice topology and unit cell (marked in dashed-shaded region) at 0°, 55°, and 70° folding angle are given in the inset (left to right), each corresponding to hexagon, square, and hexagon lattice types respectively.

a value of p equal to 9 [i.e., 361 number of plane waves for Fourier expansions of Eq. (5)], provided reliably good convergence of eigenvalues at minimum computational cost [2]. The EVP is solved along different wave vectors spanning the edges of the irreducible first Brillouin zone, and a typical band structure which represents the first few normalized eigenfrequencies along the high-symmetry directions is extracted.

B. Results and discussion

Using the PWE method described above, we extract the band structure of hexagonal-OS at a folding angle of 65°, Fig. 4(a). Three complete PBGs are found for this reduced-symmetry non-Bravais lattice. Similar calculations at different folding angles are conducted and all results are consolidated into Fig. 4(b), where the horizontal axis represents the folding angle and on the vertical axis we plot the normalized PBG edge frequencies.

To generate Fig. 4(b), a folding angle increment of 5° in 0°–45° region is used—where filling fraction is low and PBG widths are small—and a 1° increment is used in the 46°–71° region—where PBG is highly sensitive to folding angle. Results in Fig. 4(b), at standard Bravais lattice configurations viz. hexagon (0° and 70°) and square (55°) match well with existing literature [5,9]. We also validated the PBG calculations at an intermediate folding angle (65°) by comparing it against the transmission plot of hexagonal-OS generated via commercial software COMSOL (see Appendix E).

In Fig. 4(b), the PBG originating at the hexagonal lattice configuration at 0° (with midgap frequency ∼1.06, where the midgap frequency is calculated as the average of the upper and lower edge frequencies of PBG) gradually narrows with increasing folding angle and totally ceases to exist around 25°. Another PBG related to the hexagonal lattice appears at a folding angle close to 65° and starts to grow in width as the folding angle increases to 70° (midgap frequency ∼1.60). In a completely disjoint folding regime, two separate PBGs related to square lattice appear and then disappear as the folding angle increases from 50° to 66°, and their midgap frequencies are ∼0.82 and ∼2.77, respectively. Such dramatic and discrete variation in PBG spectral locations (especially in 25°–50° and 65°–66° folding regimes), together with the large PBG widths at higher folding angles make the origami structures ideal for adaptable broadband wave applications.

To gain a deeper physical insight into such discrete PBG adaptations with respect to folding, it has to be understood that during folding [see Figs. 2(c)–2(f)] (a) the lattice topology of hexagonal-OS changes between hexagon and square and (b) filling fraction increases. Figure 5 illustrates the evolution of low-frequency band gap in both hexagonal (blue markers) and square (red markers) lattices due to increase in filling fraction. It can be observed that the midgap frequency of the first band gap in both the square and hexagon symmetries form at different spectral locations for all filling fractions. Therefore, the hexagonal-OS that can undergo transformation between these two lattice symmetries during folding can observe discontinuous PBGs (black markers in Fig. 5); i.e., PBGs jump between different spectral locations as folding angle is increased (Fig. 5). Specifically, the discrete shifts in spectral location of first PBG during folding are due to the phase transformation in the hexagonal-OS's lattice topology between different symmetries. Since different lattice symmetries have different dispersion characteristics, the hexagonal-OS that is capable of shifting between them possesses rich adaptable characteristics.

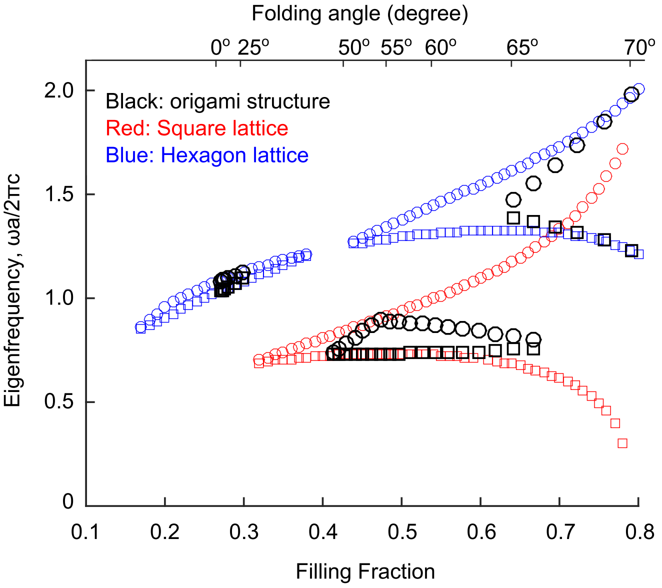

FIG. 5. Comparison of low-frequency hexagonal-OS PBGs with that of square and hexagonal lattice types. The lower (upper) edge frequencies of PBGs are represented by square (circle) markers.

C. Effect of initial lattice configuration

To study the effect of initial lattice configuration on wave adaptation behavior, we picked a different initial configuration of honeycomb (which will be referred to as honeycomb-OS)

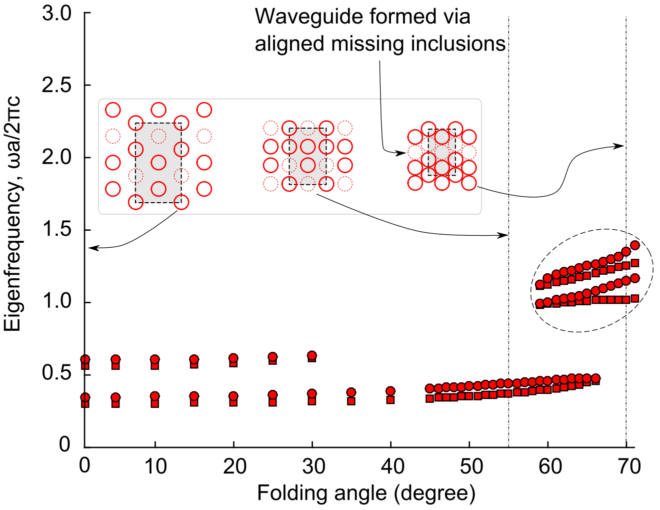

FIG. 6. PBG adaptation in OS with honeycomb as initial lattice configuration. Square (circle) markers represent the lower (upper) edge frequencies of PBG. Distribution of solid circles in the inset represent the lattice topology and dashed-shaded region represents the unit cell of honeycomb-OS at 0°, 55°, and 70° folding angles (left to right).

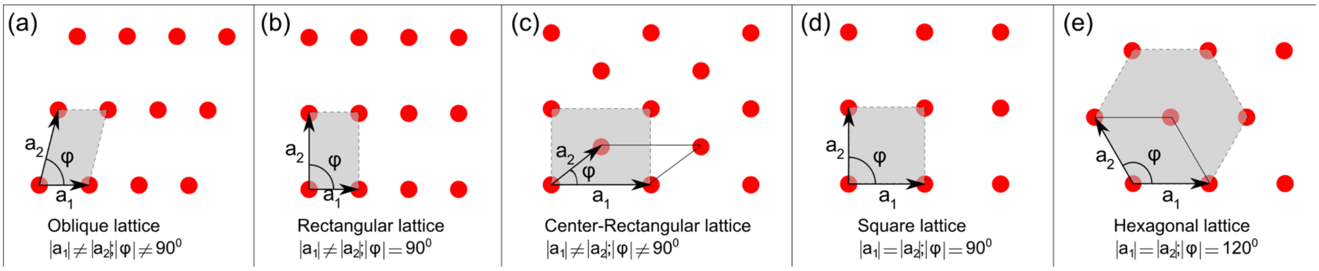

FIG. 7. (a–e) Five types of 2D Bravais lattice types.

that can be easily constructed from hexagonal-OS by simply removing a few lattice inclusions as represented by dotted circles in inset of Fig. 6. The consolidated PBG results of honeycomb-OS at different folding angles in Fig. 6 are calculated via the PWE method, with a unit cell as shown by the dashed-shaded region in the inset of Fig. 6. Further, the PBG edge frequencies on the vertical axis are reduced via the same normalization factors as used in Fig. 4(b).

In contrast to the highly sensitive PBGs of hexagonal-OS [Fig. 4(b)], the low-frequency PBG of honeycomb-OS (Fig. 6) exists for most of the folding operation and remains almost invariant. Such unique invariable transmission characteristics are never observed in topology transformation studies, and it can be useful if both the structure shape change and acoustic blocking are desired functionalities.

On another note, there are two PBGs within the area highlighted by dotted ellipse in Fig. 6, and the modes between them have localized modeshapes/wavefunctions inside the waveguide of honeycomb-OS, where the waveguide is formed via aligned missing (dotted) inclusions during the folding process. Based on previous work [17,25,26,38], these observations suggest that the two PBGs inside the dotted ellipse are created as a result of the hexagonal-OS's PBG - in the 65°–70° folding angle region [Fig. 4(b)], being split by the localized modes formed inside the waveguide of honeycomb-OS.

IV. FEATURES OF ORIGAMI STRUCTURES

The interesting wave propagation results discussed in the previous sections, both adaptive and invariant low-frequency wave properties, are all generated via folding OS with a specific Miura-Ori design [triangle crease design in Fig. 2(a)]. But because of the versatility in designing origami, as shown in Figs. 2(a) and 2(b), various other lattice topology transformations between non-Bravais lattice and different 2D Bravais lattice types (Appendix C) are also possible. Such transformations via origami folding, coupled with significant topology and symmetry variations, could lead to a large design space for tunable wave characteristics. Another key feature of OS is that its scale-independent geometric folding allows it to be fabricated at vastly different length scales without losing reconfigurability, making it a viable design for a range of spectral applications. Apart from the versatility and scalability, the global topology transformation, enabled by a 1 degree-of-freedom folding mechanism in rigid-foldable origamis, can be controlled with minimal local effort [39–44].

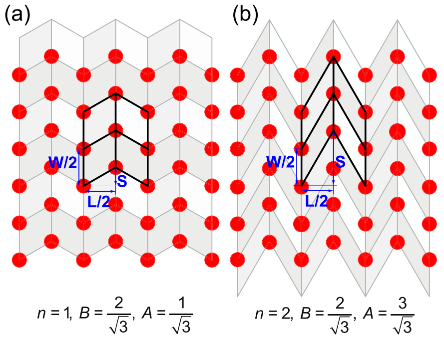

FIG. 8. (a–b) Examples illustrating two hexagonal lattices where (a) $n = 1$ and (b) $n = 2$. Even though the hexagonal lattices are identical between the two examples, the underlying Miura-Ori designs have different geometric design parameters.

V. CONCLUSION

An on-demand wave adaptation approach through exploring origami design and folding is proposed and investigated. It is shown that the unique topology transformation between distinct lattice symmetries via origami folding can cause phenomenal PBG transformation. Such drastic wave adaptability is evaluated via the PWE method and the findings are validated via transmission diagrams obtained using the commercial software, COMSOL. Apart from the radical PBG adaptation, almost invariant transmission properties are also discovered in origami structures with honeycomb as the initial lattice configuration. These interesting wave characteristics, together with the large design space, scalable geometry, and practical-to-implement actuation of origami structures, could bring on-demand wave propagation tailoring to a new level for wide spectra of acoustic applications.

ACKNOWLEDGMENTS

This research is partially supported by the University of Michigan Collegiate Professorship and the National Science Foundation under Award No. 1232436.

APPENDIX A

There are five different 2D Bravais lattice types as shown in Figs. 7(a)–7(e), viz., oblique (O), rectangle (R), center-rectangle (CR), square (S), and hexagon (H) lattice configurations. Each of the lattice types has distinct dispersion characteristics and the OS proposed in this research, which is

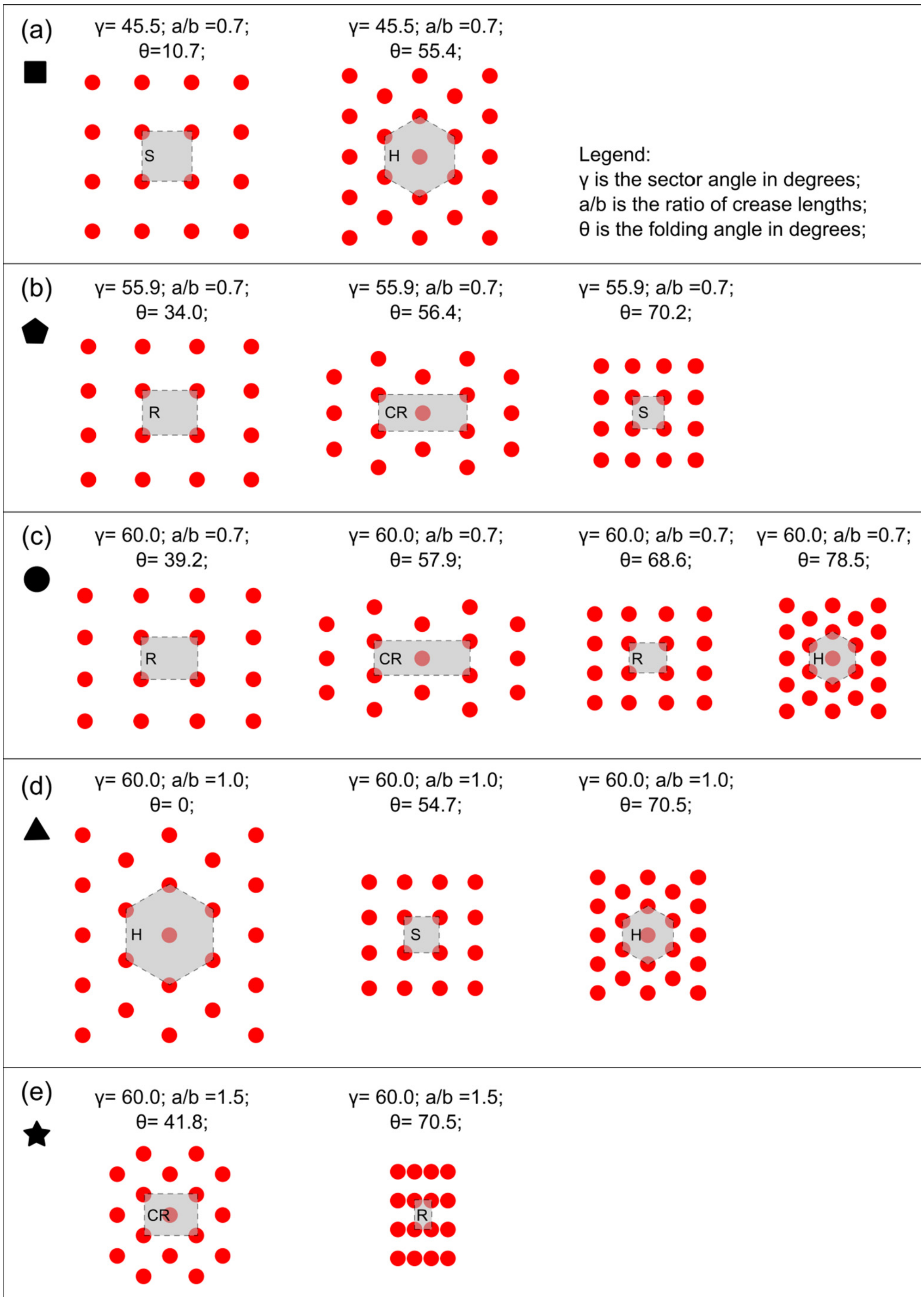

FIG. 9. (a–e) Topology transformation in OS with different Miura-Ori crease designs marked in Figs. 2(a) and 2(b).

capable of transforming its topology between different lattice types via folding, can achieve broadband PBG adaptation.

APPENDIX B

The physical significance of n in the dimensionless parameters (A and B) is explained through Figs. 8(a) and 8(b). As an example, we choose the hexagonal lattice configuration that requires $A = (2n - 1)/\sqrt{3}, B = 2/\sqrt{3}$ (where n is an integer). Even though the hexagonal lattice formed by the inclusions are identical in Figs. 8(a) and 8(b), the dimensional parameters of underlying Miura-Ori sheets that depend on unit-vertex parameters [Fig. 1(d)] are different and n is a measure of that geometry.

APPENDIX C

As an illustration of topology transformation in OS, here we show the folding-induced topology transformation in OS with five different crease designs in Figs. 9(a)–9(e). These crease designs are indicated by different markers (square, pentagon,

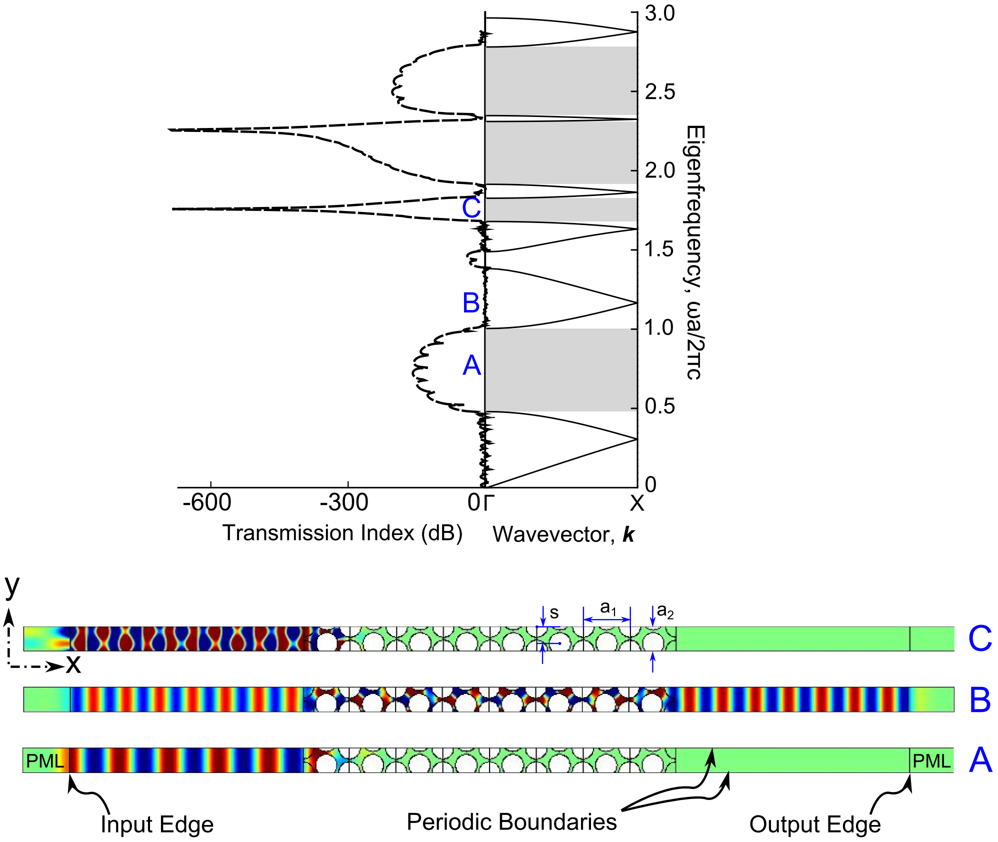

FIG. 10. Wave propagation characteristics evaluated via PWE method (right solid line) and COMSOL (left dashed line) along ΓX wave vector direction. The band gaps evaluated via PWE method along *X* direction represented by horizontal gray regions match very well with transmission dips generated via COMSOL. (A,B,C) Acoustic pressure plots at different instances along the transmission spectra demonstrating wave propagation in band gap and band pass transmission regions.

circle, triangle, and star) in Figs. 2(a) and 2(b) of the main text.

In OS with a square crease design, topology transforms between S to H [Fig. 9(a)]; in OS with pentagon crease design, topology transforms between R to CR to S [Fig. 9(b)]; in OS with circle crease design, topology transforms between R to CR to R to H [Fig. 9(c)]; in OS with triangular crease design, topology transforms between H to S to H [Fig. 9(d)], also shown in Figs. 2(c)–2(f) of main text; and finally in OS with star crease design, topology transforms between CR to R [Fig. 9(e)].

With the parametric analysis results shown in Figs. 2(a) and 2(b) and the folding illustrations shown here in Figs. 9(a)–9(e), we can conclude that the OS with Miura-Origami design can be designed to transform between the four Figs. 7(b)–7(e) of the five Bravais lattices.

APPENDIX D

The Fourier coefficient $\boldsymbol{\tau_G}$ in Eq. (5) for circular inclusion can be simplified as given in Eq. (D1), where J is the Bessel function of the first kind of order 1, "*inc*" representing the equivalent inclusions, *BG* referring to the host media, and *R* the radius of the circular inclusion:

$$\tau_{\vec{G}=0} = \frac{1}{A_{\text{cell}}}\left\{\sum_{\text{inc}=1}^{\text{total inclusons}} [A_{\text{inc}}(\tau_{\text{inc}}-\tau_{BG})] + A_{\text{cell}}\tau_{BG}\right\},$$

$$\tau_{\vec{G}\neq 0} = \frac{1}{A_{cell}}\left\{\sum_{\text{inc}=1}^{\text{total inclusons}} \left[J(|\vec{G}|R_{\text{inc}})e^{-i\vec{G}\cdot\vec{C}_{\text{inc}}}\frac{2\pi}{|\vec{G}|}(\tau_{\text{inc}}-\tau_{BG})R_{\text{inc}}\right]\right\}. \tag{D1}$$

APPENDIX E

To validate the dispersion characteristics presented in the main text, here we evaluate the transmission spectra of finite hexagonal-OS at 65° folding along the *X*-direction via commercial software COMSOL; the results are compared against the band structure (along Γ*X* direction) obtained using PWE method. In this spirit, the cross section of periodically distributed circular steel rods in air at 65° folding angle

[Fig. 2(e)] are modeled in the acoustic-structural interaction module of COMSOL as a strip with finite length and periodic boundaries along the X and Y directions, respectively (refer to the bottom panel of Fig. 10). The following are the geometric parameters of the COMSOL model: unit-cell lengths along X and Y direction are $a_1 = 0.177\,2[\mathrm{m}]$ and $a_2 = 0.092\,9[\mathrm{m}]$, respectively, the radius of steel inclusion is 0.041[m], and the staggered distance between the two adjacent columns of inclusions is $s = 0.028[\mathrm{m}]$. To evaluate the X-direction wave propagation behavior, a plane pressure wave is applied as input on the left edge and perfectly matched layers (PMLs) are applied to the left and right edges to avoid reflections. Through the frequency domain analysis, the transmission spectrum—defined as the output to input ratio of the sound pressure level (dB)—is extracted and shown as a dashed curve in the top-left corner of Fig. 10. In the interest of comparison, in Fig. 10 we also provide the band structure (represented by a solid line) predicted using the PWE method [dispersion curves in Fig. 4(a) along ΓX direction]. From the top two curves in Fig. 10 (dotted and solid), it is clearly evident that the transmission dips generated via COMSOL correspond very well with the band gaps predicted via PWE along the ΓX wave vector. Also, the steady-state acoustic pressure maps at different points along the transmission spectra (e.g., A, B, and C in Fig. 10) clearly illustrate the wave blocking and propagation phenomena. Thus the COMSOL simulation serves as a way to validate the PWE method and also provides a tool to extract the magnitude of transmission and sound pressure distribution inside the OS at a chosen frequency. The attenuations in transmission spectra of semi-infinite phononic structures derived here via numerical analysis (Fig. 10) are comparable to attenuation magnitudes reported in other recent literature [19].

[1] M. S. Kushwaha, P. Halevi, G. Martinez, L. Dobrzynski, and B. Djafari-Rouhani, Phys. Rev. B **49**, 2313 (1994).

[2] M. S. Kushwaha, Appl. Phys. Lett. **70**, 3218 (1997).

[3] M. M. Sigalas and E. N. Economou, Europhys. Lett. **36**, 241 (1996).

[4] J. V. Sánchez-Pérez, D. Caballero, R. Mártinez-Sala, C. Rubio, J. Sánchez-Dehesa, F. Meseguer, J. Llinares, and F. Gálvez, Phys. Rev. Lett. **80**, 5325 (1998).

[5] D. Caballero, J. Sánchez-Dehesa, C. Rubio, R. Mártinez-Sala, J. V. Sánchez-Pérez, F. Meseguer, and J. Llinares, Phys. Rev. E **60**, R6316 (1999).

[6] C. Rubio, D. Caballero, J. V. Sánchez-Pérez, R. Mártinez-Sala, J. Sánchez-Dehesa, F. Meseguer, and F. Cervera, J. Light. Technol. **17**, 2202 (1999).

[7] D. Caballero, J. Sánchez-Dehesa, R. Mártinez-Sala, C. Rubio, J. V. Sánchez-Pérez, L. Sanchis, and F. Meseguer, Phys. Rev. B **64**, 064303 (2001).

[8] Y. Lai, X. Zhang, and Z.-Q. Zhang, Appl. Phys. Lett. **79**, 3224 (2001).

[9] Y. Lai, X. Zhang, and Z.-Q. Zhang, J. Appl. Phys. **91**, 6191 (2002).

[10] J. V. Sánchez-Pérez, C. Rubio, R. Mártinez-Sala, R. Sánchez-Grandia, and V. Gomez, Appl. Phys. Lett. **81**, 5240 (2002).

[11] S. Yang, W.-D. Yu, and N. Pan, Physica B **406**, 963 (2011).

[12] L. Zhong, F. Wu, X. Zhang, H. Zhong, and S. Zhong, Phys. Lett. A **339**, 164 (2005).

[13] Z. Xu, F. Wu, Z. Mu, X. Zhang, and Y. Yao, J. Phys. D. Appl. Phys. **40**, 5584 (2007).

[14] Y. Yao, Z. Hou, and Y. Liu, Phys. Lett. A **362**, 494 (2007).

[15] R. Wei, B. Wu, C. He, and H. Zhao, Physica B **404**, 3795 (2009).

[16] X.-F. Li, X. Ni, L. Feng, M.-H. Lu, C. He, and Y.-F. Chen, Phys. Rev. Lett. **106**, 084301 (2011).

[17] V. Romero-García, C. Lagarrigue, J.-P. Groby, O. Richoux, and V. Tournat, J. Phys. D **46**, 305108 (2013).

[18] C. Rubio, A. Uris, P. Candelas, F. Belmar, and V. Gomez-Lozano, AIP Adv. **5**, 057150 (2015).

[19] J. S. Lee, S. Yoo, Y. K. Ahn, and Y. Y. Kim, J. Acoust. Soc. Am. **138**, EL217 (2015).

[20] S. Babaee, J. T. B. Overvelde, E. R. Chen, V. Tournat, and K. Bertoldi, Sci. Adv. **2**, e1601019 (2016).

[21] H. Yasuda, C. Chong, E. G. Charalampidis, P. G. Kevrekidis, and J. Yang, Phys. Rev. E **93**, 043004 (2016).

[22] K. Fuchi, J. Tang, B. Crowgey, A. R. Diaz, E. J. Rothwell, and R. O. Ouedraogo, IEEE Antenn. Wireless Propag. Lett. **11**, 473 (2012).

[23] K. Fuchi, A. R. Diaz, E. J. Rothwell, R. O. Ouedraogo, and J. Tang, J. Appl. Phys. **111**, 084905 (2012).

[24] T. Gorishnyy, M. Maldovan, C. Ullal, and E. Thomas, Phys. World **18**, 24 (2005).

[25] T. Miyashita, Meas. Sci. Technol. **16**, R47 (2005).

[26] Y. Pennec, J. O. Vasseur, B. Djafari-Rouhani, L. Dobrzyński, and P. A. Deymier, Surf. Sci. Rep. **65**, 229 (2010).

[27] M. Maldovan, Nature (London) **503**, 209 (2013).

[28] A. Gupta, Acoust. Phys. **60**, 223 (2014).

[29] R. Fleury, D. L. Sounas, M. R. Haberman, and A. Alù, Acoust. Today **11**, 14 (2015).

[30] E. D. Demaine and J. O. Rourke, *Geometric Folding Algorithms: Linkages, Origami, Polyhedra*, 1st ed. (Cambridge University Press, New York, 2007).

[31] M. McArthur and R. J. Lang, *Folding Paper* (Tuttle Publishing, North Clarendon, VT, 2010).

[32] D. Dureisseix, Int. J. Space Struct. **27**, 1 (2012).

[33] A. Lebée, Int. J. Space Struct. **30**, 55 (2015).

[34] S. Li, H. Fang, and K. W. Wang, Phys. Rev. Lett. **117**, 114301 (2016).

[35] H. Fang, S. Li, and K. W. Wang, Proc. R. Soc. London, Ser. A (2016).

[36] H. Fang, S. Li, H. Ji, and K. W. Wang, Phys. Rev. E **94**, 043002 (2016).

[37] See Supplemental Material at http://link.aps.org/supplemental/10.1103/PhysRevB.95.064307 for animation of topology transformation between hexagon and square lattice topologies in origami structure during folding.

[38] A. Khelif, A. Choujaa, S. Benchabane, V. Laude, and B. Djafari-Rouhani, IEEE Ultrason. Symp. **1**, 654 (2004).

[39] S. Li and K. W. Wang, J. Intell. Mater. Syst. Struct. **23**, 291 (2012).

[40] S. Li and K. W. Wang, Smart Mater. Struct. **22**, 014001 (2013).

[41] S. Li and K. W. Wang, Smart Mater. Struct. **24**, 105031 (2015).

[42] S. Li and K. W. Wang, J. R. Soc. Interface **12**, 20150639 (2015).

[43] M. Piñeirua, J. Bico, and B. Roman, Soft Matter **6**, 4491 (2010).

[44] P. von Lockette and R. Sheridan, *ASME Smart Materials, Adaptive Structures and Intelligent Systems Conference*, Vol. 1 (ASME, 2013), p. V001T01A020.